PAPER

(●) Check for updates

Hybrid structured $CoNi_2S_4/Ni_3S_2$ nanowires with multifunctional performance for hybrid capacitor electrodes and overall water splitting

Xiaoyun Liu, (ID) *[a] Qian Li,[a] Xin Zhang[c] and Yueqiu Jiang*[b]

Rational design of electrode materials plays a significant role in potential applications such as energy storage and conversion. In this work, $CoNi_2S_4/Ni_3S_2$ nanowires grown on Ni foam were synthesized through a facile hydrothermal approach, revealing a large capacitance of 997.2 F g^{-1} and cycling stability with 80.3% capacitance retention after 5000 cycles. The device was prepared using $CoNi_2S_4/Ni_3S_2$//AC as the positive electrode and active carbon as the negative electrode, and delivered an energy density of 0.4 mW h cm^{-3} at a power density of 3.99 mW cm^{-3} and an excellent cycle life with 79.2% capacitance retention after 10 000 cycles. In addition, the hybrid $CoNi_2S_4/Ni_3S_2$ nanowires demonstrate excellent OER performance with low overpotential of 360 mV at 30 mA cm^{-2} and overpotential of 173.8 mV at -10 mA cm^{-2} for the HER, a cell voltage of 1.43 V, and excellent cycle stability.

1. Introduction

In recent years, various transition metal-based catalysts such as phosphides, oxides, nitrides, carbides, and sulfides have been widely investigated as excellent electrochemical catalysts but the improvement of bi-functional electrocatalysts with excellent HER and OER activity is still difficult and slow to implement.[1–4] To date, as demonstrated by experiments, electrocatalysts with vertically well-aligned arrays on 1D nanostructures consistently lead to improved HER and OER activity and promise efficient overall water splitting.[5,6] Nanostructures possess distinctive advantages, including easier electrolyte diffusion and ionic transportation, better electrical connection with substrates, and offer larger surface area to provide contact between the electrode and electrolyte.[7] Special nanostructures possess interconnected networks; these hierarchical heterostructures allow for efficient electron/ion transportation and accommodate volume variation nicely. Meanwhile, heterostructures consist of highly conductive materials as the "substratum" and transition metal oxides as the "superstratum"; thus, the combination of the two types of active materials create heterostructures that inherit advantages from both the "substratum" and "superstratum".[8–10] As highlighted in recent reports, $Ni(OH)_2/Ni_3S_2$ nanostructure arrays on Ni foam show excellent electrochemical activity with a low overpotential of 270 mV (OER) at 20 mA cm^{-2} in 1.0 M KOH but exhibited a low

HER activity (211 mV at 10 mA cm^{-2}).[11] Zhao *et al.* prepared nitrogen-doped carbon nanomaterials as efficient oxygen evolution electrocatalysts, which exhibited an overpotential of 380 mV at a current density of 10 mA cm^{-2} in alkaline media.[12] An effective design of catalysts integrating HER and OER activity materials is the key for overall water splitting.[13] Recently, benefits from cobalt include better redox activity under mild reaction conditions, modest overpotential, and the extremely high theoretical rich polymorphism of molybdenum, Co-based electrode materials have demonstrated vastly improved electrochemical performance.[14,15]

Among various electrode materials, spinel-structured $CoNi_2O_4$ has been investigated due to the high theoretical capacitance, high electrochemical performance and excellent electrocatalytic performance.[16,17] For example, Tong *et al.* reported $CoNi_2O_4$ nanoneedles through a simple hydrothermal method. The as-prepared samples exhibited a specific capacitance of 1192 mF cm^{-2} at 2 mA cm^{-2} and cycle stability.[18] Liu and co-workers prepared $NiCo_2O_4$ nanowires through a simple hydrothermal process; the as-prepared samples showed excellent electrocatalytic performance with an overpotential of 320 mV at 10 mA cm^{-2}.[19] However, single metal oxide electrode materials often present poor electrical conductivity, which limits the electrochemical performance. To improve the electrical conductivity, constructing a hybrid structure with metal sulfides has been considered an efficient method due to the improved electrical conductivity (about 100 times) over corresponding single metal oxides and binary materials.[20] In the literature, Li *et al.* fabricated $NiCo_2S_4$@$Co(OH)_2$ core–shell nanotube arrays, which showed an area capacitance of 9.6 F cm^{-2} at 2 mA cm^{-2}.[21] Jiang *et al.* prepared $NiCo_2S_4$@NiFe LDH heterostructures through a simple method, and the as-prepared

[a]*School of Science, Shenyang Ligong University, Shenyang 110159, P. R. China. E-mail: liuxy@imr.ac.cn*

[b]*Department of Development and Planning, Shenyang Ligong University, Shenyang 110159, P. R. China. E-mail: yueqiujiang@sylu.edu.cn*

[c]*School of Automobile and Transportation, Shenyang Ligong University, Shenyang 110159, P. R. China*

electrocatalysts showed an overpotential of 201 mV and excellent cycle stability.[22]

Herein, we successfully synthesize $CoNi_2O_4/Ni_3S_2$ nanowires on Ni foam through a facile hydrothermal route. The as-fabricated samples deliver a high specific capacitance of 997.2 $F g^{-1}$ at 1 $A g^{-1}$ and cycle stability. In addition, the device exhibits an energy density of 0.4 $mW h cm^{-3}$ at a power density of 3.99 $mW cm^{-3}$ and an excellent cycle life with 79.2% capacitance retention after 10 000 cycles. As electrocatalysts, the hybrid $CoNi_2S_4/Ni_3S_2$ nanowires show excellent OER performance with a low overpotential of 360 mV and a small Tafel slope of 69.7 mV dec^{-1}, and overpotential of 173.8 mV for the HER and Tafel slope of 98.8 mV dec^{-1} and excellent cycle stability.

2. Experimental section

2.1. Material preparation

Firstly, Ni foam was pre-treated *via* immersion in 0.1 M HCl, absolute ethanol and deionized water, respectively. Then, 1 mM $Ni(NO_3)_2 \cdot 6H_2O$, 2 mM $Co(NO_3)_2 \cdot 6H_2O$, 4 mM NH_4F and 10 mM urea were dissolved in 60 mL deionized water. Then, the solution was transferred into an 80 mL Teflon-lined autoclave and kept at 120 °C for 8 h. Then, the samples were washed several times. Finally, the $CoNi_2O_4$ nanowires were obtained after calcination at 350 °C for 2 h (the average mass loading was 1.8 mg cm^{-2}). Secondly, 0.35 g Na_2S was dissolved into 40 mL deionized water and kept at 120 °C for 4 h. After cooling down to room temperature, the as-fabricated products were washed and dried at 60 °C. The average mass loading was 3.2 mg cm^{-2}.

2.2. Materials characterization

The crystallographic structure of the as-fabricated samples was measured through X-ray diffraction. The morphology and structure of the samples were characterized by using scanning electron microscopy (SEM, Hitachi-4800) and high resolution transmission electron microscopy (HRTEM, JEM-2100 PLUS). X-ray photoelectron spectroscopy (XPS) measurements were conducted to investigate the element composition using an ESCA-LAB250 with Al Kα sources.

2.3. Electrochemical measurement

Electrochemical measurements of the as-prepared products including cyclic voltammetry (CV) curves, galvanostatic charge–discharge (GCD) and electrochemical impedance spectroscopy (EIS) were carried out by a CHI660e electrochemical workstation in a three-electrode system in 3.0 M KOH solutions. The as-fabricated samples ($d = 1$ cm) were used as the working electrode, Pt foil served as the counter electrode and Hg/HgO as the reference electrode. Electrochemical impedance spectroscopy (EIS) measurements were conducted in a frequency range from 0.01 to 100 kHz at a 5 mV open circuit potential. The specific capacitance of the as-prepared samples was calculated from GCD curves *via* the following equations;

$$C_s = I\Delta t/mV \quad (1)$$

where C_s, I, Δt, V and m are the specific capacitance ($F g^{-1}$), current density (A), discharge time (s), voltage (V) and mass loading (mg), respectively.

2.4. Fabrication of the hybrid battery

A hybrid battery was assembled with active carbon as the negative electrode, the as-fabricated $CoNi_2S_4/Ni_3S_2$ nanowires as the positive electrode and PVA–KOH gel as the electrolyte. PVA–KOH gel as the electrolyte was prepared as follows: 3 g PVA was added in 25 mL deionized water at 65 °C. Then, 3 g KOH was dissolved in 5 mL deionized water and added to the above solution.

2.5. Electrocatalytic performance of the hybrid battery

OER and HER performance tests of the as-prepared device were conducted in the three-electrode system. The as-fabricated samples were the working electrodes, and Ag/AgCl was the reference electrode. A graphite rod was the counter electrode. Overall water splitting was measured in a two-electrode system. All potentials were converted to reversible hydrogen electrode (RHE) though the Nernst equation $E_{RHE} = E_{Ag/AgCl} + 0.197 + 0.059 \times pH$, where $E_{Ag/AgCl}$ is the measured potential.

3. Results and discussion

Fig. 1 shows the synthesis diagram of the hybrid $CoNi_2S_4//Ni_3S_2$ nanowires through a two-step hydrothermal process. Firstly, $CoNi_2O_4$ products were fabricated on the surface of Ni foam through a simple hydrothermal process. Then, the hybrid $CoNi_2S_4/Ni_3S_2$ products were prepared by an *in situ* vulcanization process.

Fig. 2a shows the crystal structure of the samples; the diffraction peaks at 2θ values of 44.4, 51.6 and 76.1 degrees can be indexed to Ni foam (JCPDS no. 04-0850). The diffraction peaks at 2θ values of 31.4, 38.2, 50.3, 55.0 and 64.8 degrees could be ascribed to the (311), (400), (511), (440) and (533) crystal planes of spinel $CoNi_2S_4$ phase (JCPDS no. 24-0334). In addition, the diffraction peaks at 31.1, 37.8, 44.3, 50.1 and 55.2 degrees could be indexed to the (110), (003), (202), (211) and (300) crystal planes of Ni_3S_2 (JCPDS no. 44-1418), respectively, which can be attributed to the vulcanization of the Ni foam. XPS analyses were used to further investigate the chemical composition and valence. Fig. 2b shows the XPS full survey spectrum of the $CoNi_2S_4//Ni_3S_2$ nanowires, and the products consisted of Ni, Co and S. The Co 2p spectrum (Fig. 2c) contains two spin–orbit doublets and two shakeup satellites, the binding energy at 779.2 and 795.1 eV could be ascribed to Co^{3+}, and the binding energies at 780.9 and 795.3 eV belong to the Co^{2+} phase.[23] In addition, the satellite peaks reveal that Co^{3+} is present.[24] Fig. 2d shows the Ni 2p spectrum, which can be divided into two spin–orbit doublets and two shakeup satellites. The binding energies at 854.8 and 871.6 eV can be assigned to Ni^{3+} and 854.3 and 871.2 eV are Ni^{2+}.[25] The sharp intense satellite peaks indicate that Ni is present as Ni^{2+}.[26] The S 2p spectrum is presented in Fig. 2e. The peak at 161.2 eV is S $2p_{1/2}$ and the peak at 162.3 eV belongs to a typical metal–sulfur bond, which improves the electrochemical
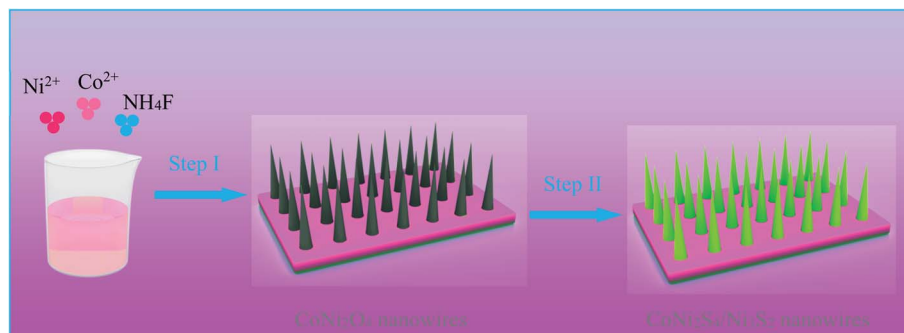
Fig. 1 Schematic illustration of the fabrication process of CoNi$_2$S$_4$/Ni$_3$S$_2$ nanowires.

activity of the as-prepared samples.[27,28] Energy-dispersive X-ray spectrometry (EDX) measurements of the as-prepared CoNi$_2$S$_4$/Ni$_3$S$_2$ nanowires indicate that the as-fabricated products are composed of Ni, Co and S, as shown in Fig. 2f, and the three elements are uniformly distributed on the surface of the as-prepared samples, revealing that CoNi$_2$S$_4$/Ni$_3$S$_2$ nanowires are uniformed deposited on the surface of Ni foam.

The morphology characteristics of the as-synthesized CoNi$_2$S$_4$/Ni$_3$S$_2$ nanowires were first characterized through SEM. From the low magnification SEM images in Fig. 3a, it is clearly found that CoNi$_2$S$_4$/Ni$_3$S$_2$ nanowires are uniformly located on the surface of Ni foam. From Fig. 3b, it can be found that adjacent nanowires are connected to each other to form a network structure. Fig. 3c presents high magnification SEM images, indicating that the as-prepared CoNi$_2$S$_4$/Ni$_3$S$_2$ nanowires possess an average diameter of 75 nm. TEM measurements were used to further characterize the microstructures of CoNi$_2$S$_4$/Ni$_3$S$_2$ nanowires. Fig. 3d exhibits the low-magnification

TEM images of the as-fabricated samples, in which a single nanowire is made of some tiny nanoparticles and the samples show the average diameter of 70 nm. The HRTEM image shows that the lattice spacing of 0.321 nm matches well with the (220) plane of Ni$_3$S$_2$ phase, and the lattice spacing of 0.283 nm can be indexed to the (311) plane of CoNi$_2$S$_4$ spinel structure. As can be seen from Fig. 3e, it can further confirmed that the as-prepared samples contain CoNi$_2$S$_4$ and Ni$_3$S$_2$ phases, which is consistent with the XRD patterns. The SAED pattern illustrated in Fig. 3f, shows that the as-fabricated samples present polycrystalline features that possess more active sites and energy barriers for adsorbing water molecules.

To investigate the electrochemical performances of the as-prepared samples, Fig. 4a exhibits the CV curves of CoNi$_2$O$_4$ samples at scan rates from 5 to 50 mV s^{-1}. It is seen that CV curves show a pair of redox peaks, demonstrating that the products possess typical pseudocapacitive characteristics. Fig. 4b shows the GCD curves of the CoNi$_2$S$_4$/Ni$_3$S$_2$ samples, and it is seen that the

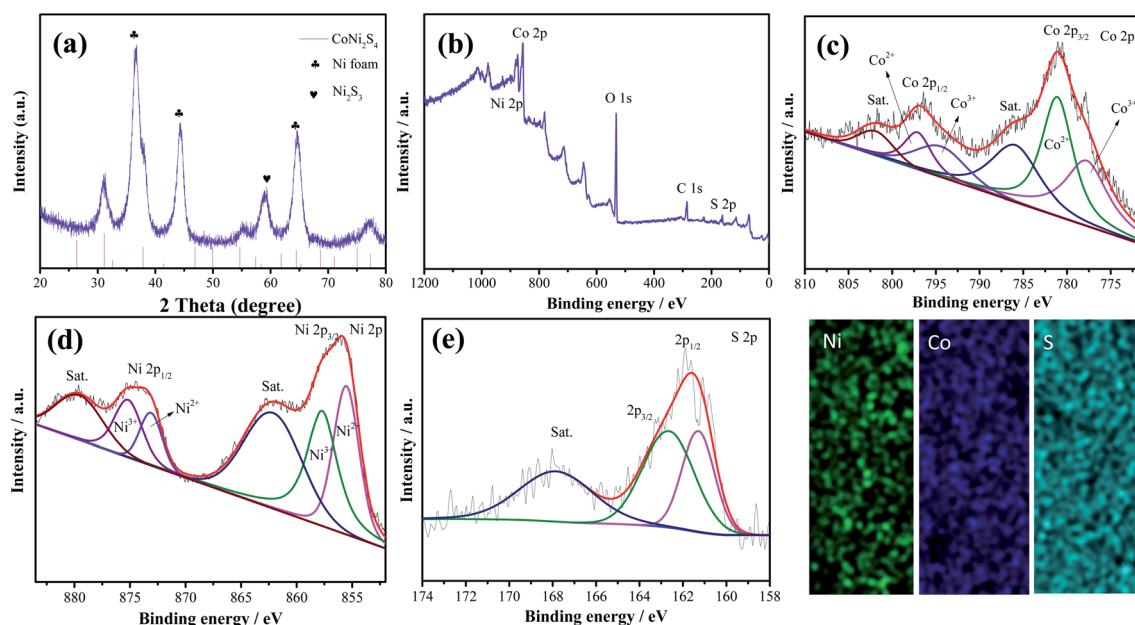Fig. 2 (a) XRD pattern of the as-fabricated CoNi$_2$S$_4$/Ni$_3$S$_2$ nanowires. (b) Survey spectra of the samples (c) Co 2p, (d) Ni 2p and (e) S 2p. (f) Elemental mapping.
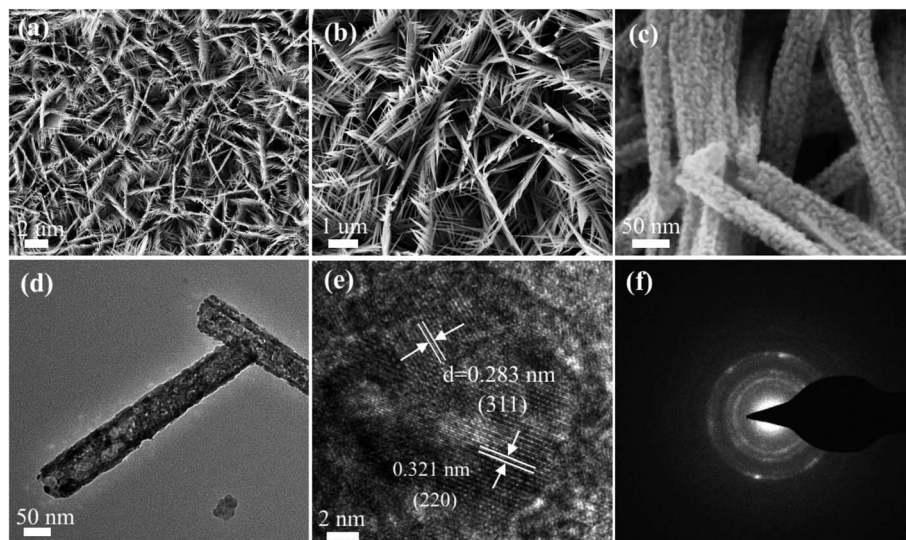
Fig. 3 SEM images of the as-fabricated $CoNi_2S_4/Ni_3S_2$ nanowires. (a and b) Low magnification and (c) high magnification images. (d) TEM images. (e) HRTEM images. (f) SAED images.

samples possess a specific capacitance of 997.2 F g^{-1} at a current density of 1 A g^{-1}. CV curves of the hybrid $CoNi_2S_4/Ni_3S_2$ samples are depicted in Fig. 4c, and it is observed that the integrated areas

increase as the scan sweep increases, indicating that the as-fabricated samples possess a fast ion and electron transfer rate. Based on previous reports, Ni foam contributes little to the
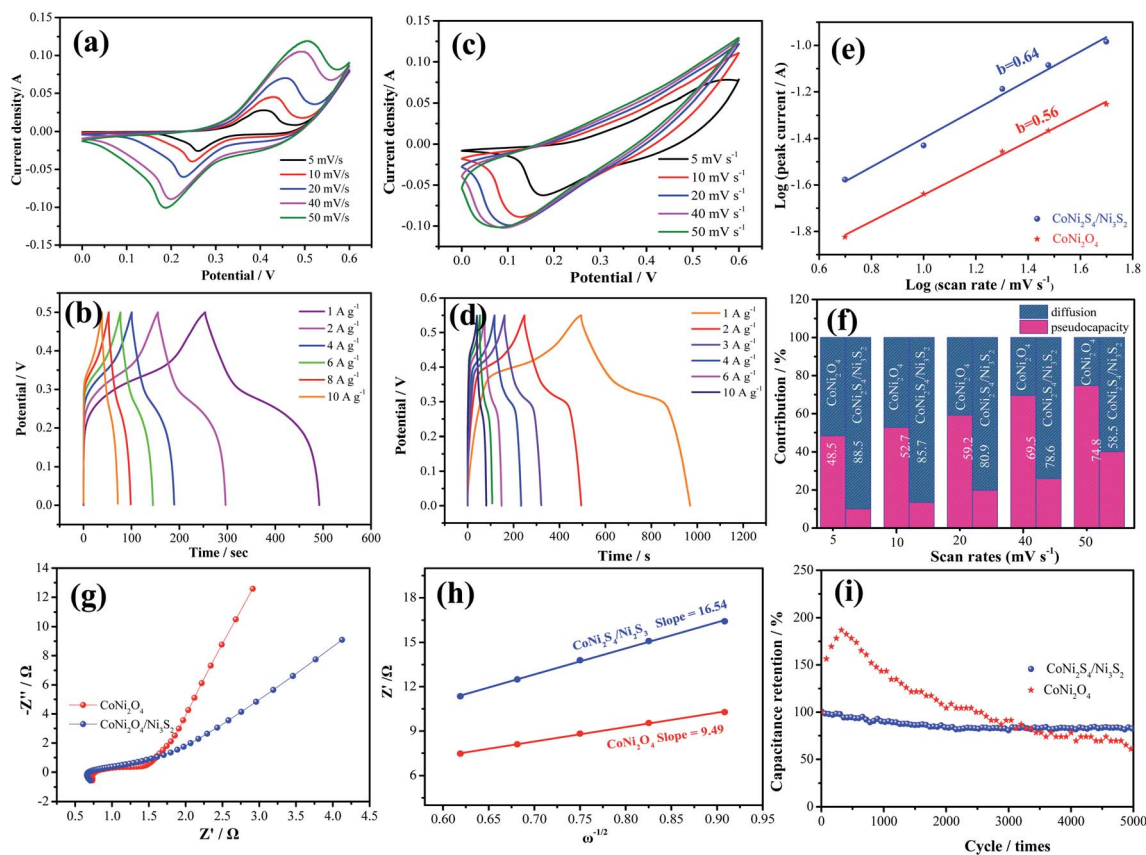

Fig. 4 Electrochemical performance measurements. (a) CV curves of $CoNi_2O_4$, (b) GCD curves of $CoNi_2O_4$ samples, (c) CV curves of $CoNi_2S_4/Ni_3S_2$, (d) GCD curves of $CoNi_2S_4/Ni_3S_2$, (e) b values of two kinds of electrode materials, (f) capacitance contribution ratio, (g) Nyquist plots, (h) Z' as a function of $\omega^{-1/2}$ plot in low frequency, (i) cycling stability tests.

capacitance.[29] Fig. 4d shows the GCD curves of the as-prepared electrode at different current densities from 1 A g^{-1} to 10 A g^{-1}. It is found that the as-fabricated samples exhibit a high specific capacitance of 997.2 F g^{-1} at 1 A g^{-1}. To further analyze the electrochemical kinetics of the as-prepared samples, the capacitance can be calculated according to following equation:

$$i = av^b \tag{2}$$

where a and b are constants. The b value of 0.5 and 1.0 represent capacitive behavior and battery behavior, respectively. The b value (Fig. 4e) for reduction peaks of CoNi$_2$O$_4$ and CoNi$_2$S$_4$/Ni$_3$S$_2$ electrodes is 0.64 and 0.56, respectively. In addition, the capacitive contribution ratio can be obtained through the following equation:[30]

$$i = k_1\nu + k_2\nu^{1/2} \tag{3}$$

where i, ν, k_1 and k_2 represent the current, scan rates and the constant, respectively. Fig. 4f shows the calculated pseudocapacitance and diffusion-controlled capacitance at scan rates from 5 to 50 mV s^{-1}. It is seen that the contribution of diffusion-controlled capacity gradually decreases with increasing scan rate, indicating that the samples show fast transmission for OH$^-$. At the same time, the pseudocapacitance arrives at the highest value of 74.8% at 50 mV s^{-1}. EIS is used to further investigate the electrochemical performance, as shown in Fig. 4g. It is obvious that the intercept at the real axis shows the R_s value of CoNi$_2$S$_4$/Ni$_3$S$_2$ nanowires of 0.61 Ω. The underlying mechanism of differences in the capacitance performance of different samples was explored in the corresponding Nyquist

curves, as shown in the inset of Fig. 4g. The CoNi$_2$S$_4$/Ni$_3$S$_2$ electrode showed lower contact resistance and charge transfer resistance than the CoNi$_2$O$_4$ nanowires, further confirming that the hybrid structure possesses excellent electrochemical performance. Simultaneously, in order to study the reaction kinetics in the low frequency region, the spectrum can be fit using the following equation:

$$Z = R_s + R_{ct} + \sigma_w\omega^{-1/2} \tag{4}$$

where σ_w is the Warburg factor and ω is angular frequency. Z can be attributed to the diffusive resistance of OH$^-$. The values of CoNi$_2$O$_4$ and CoNi$_2$S$_4$/Ni$_3$S$_2$ electrodes are 16.54 and 9.49, respectively, indicating that CoNi$_2$S$_4$/Ni$_3$S$_2$ samples possess a fast transmission for OH$^-$ (Fig. 4g). The cycling stability of the as-fabricated samples is measured by GCD measurements, as illustrated in Fig. 4i, revealing that the as-prepared CoNi$_2$S$_4$/Ni$_3$S$_2$ sample shows more excellent stability with 80.3% capacitance retention than CoNi$_2$O$_4$ samples (64.2%) after 5000 cycles.

To further investigate the practical application of the as-fabricated electrode, the device is assembled with the CoNi$_2$S$_4$/Ni$_3$S$_2$ nanowires electrode as the positive electrode and active carbon as the negative electrode. The composition of CV curves of the CoNi$_2$S$_4$/Ni$_3$S$_2$ nanowires and active carbon at a current density of 50 mV s^{-1} are depicted in Fig. 5a. It is found that the electrode materials exhibit single potential windows of −1.0–0 V and 0–0.6 V, respectively, indicating that the device can reach a total potential of 1.6 V. Fig. 5b exhibits the CV curves of the fabricated CoNi$_2$S$_4$/Ni$_3$S$_2$ nanowires//AC device at scan rates from 2 to 50 mV s^{-1}. It can be seen that the device can
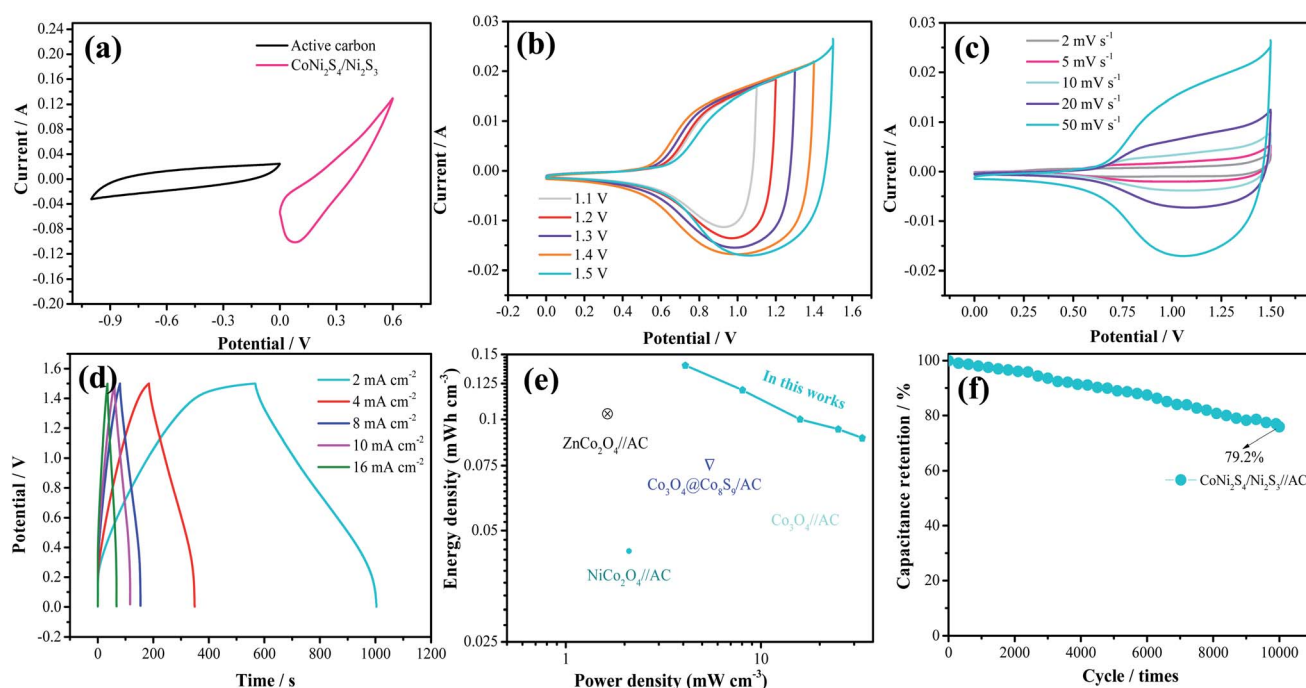

Fig. 5 Electrochemical performance characteristics of the as-fabricated device. (a) The CV comparison of CoNi$_2$S$_4$/Ni$_3$S$_2$//AC, (b) CV curves at different potential window, (c) CV curves, (d) GCD curves, (e) Ragone plots, (f) cycling stability measurements.
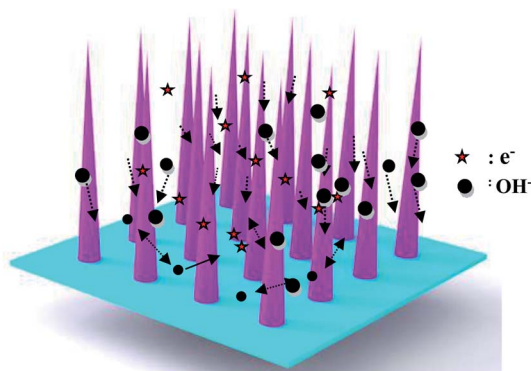
Fig. 6 Electrochemical mechanism diagram of the $CoNi_2S_4/Ni_3S_2$ samples.

work in a voltage window of 0–1.5 V. With increasing scan rates, the CV shapes are maintained, indicating that the capacitors possess excellent rate performance. CV curves of the $CoNi_2S_4/Ni_3S_2$ nanowires//AC device with different potential windows at a scan rate of 50 mV s^{-1} are collected to investigate the extended working voltage, as illustrated in Fig. 5c, and the device shows a stable capacitive behavior with electric double-layer capacitive properties even at a voltage of up to 1.5 V. Fig. 5d shows the GCD measurement of the device, which showed that the areal capacitance of the $CoNi_2S_4/Ni_3S_2$ nanowires//AC device reaches 136.05 mF cm^{-2} at a current density of 2 mA cm^{-2}. As the current density increased to 10 mA cm^{-2}, the areal capacitance was maintained at 56 mF cm^{-2}. The Ragone plots of the asymmetric supercapacitors are shown in Fig. 5e. The $CoNi_2S_4/Ni_3S_2$ nanowires//AC supercapacitors deliver a maximum energy

density of 0.4 mW h cm^{-3} at a power density of 3.99 mW cm^{-3}, which is comparable to previously reported ASC devices.[31–34] The long-term cycling stability of the $CoNi_2S_4/Ni_3S_2$ nanowires//AC device is also evaluated by repeating charge–discharge measurements, as shown in Fig. 5f. After 10 000 cycles, there is still 90% retention of the original capacitance at a current density of 5 mA cm^{-2}.

The as-fabricated samples possess excellent cycle stability, which can be ascribed to the following aspects, as shown in Fig. 6. First, the as-fabricated $CoNi_2S_4/Ni_3S_2$ nanowires are directly on Ni foam, which provides a lot of active sites. Secondly, the hybrid $CoNi_2S_4/Ni_3S_2$ structure alleviates the volume change during the electrochemical reaction process. Finally, the adjacent nanowires possess enough reaction space, which leads to a rapid electrochemical reaction.

The electrocatalytic performance of the as-prepared catalysts is estimated through LSV and Tafel curves in 1.0 M KOH solution. As shown in Fig. 7a, the hybrid $CoNi_2S_4/Ni_3S_2$ nanowires show a lower overpotential of 360 mV compared to that of $CoNi_2O_4$ nanowires (380 mV), Ni_3S_2 samples (410) and Ni foam (459 mV) at a current density of 30 mA cm^{-2}, which demonstrates that $CoNi_2S_4/Ni_3S_2$ nanowires possess better electrocatalytic performance. To give insight into the OER kinetic mechanism, Fig. 7b presents the Tafel slope of the catalyst. Hybrid $CoNi_2S_4/Ni_3S_2$ nanowires exhibit a small Tafel slope of 69.7 mV dec^{-1}, which is lower than that of the $CoNi_2O_4$ nanowires (71.5 mV dec^{-1}), Ni_3S_2 samples (83.2 mV dec^{-1}) and Ni foam (135.3 mV dec^{-1}). The low Tafel slope increases the charge transfer rate and provides active sites for OH adsorption.[35] To further study the outstanding OER activity, the electrochemical active surface area (ECSA) was measured through the double-
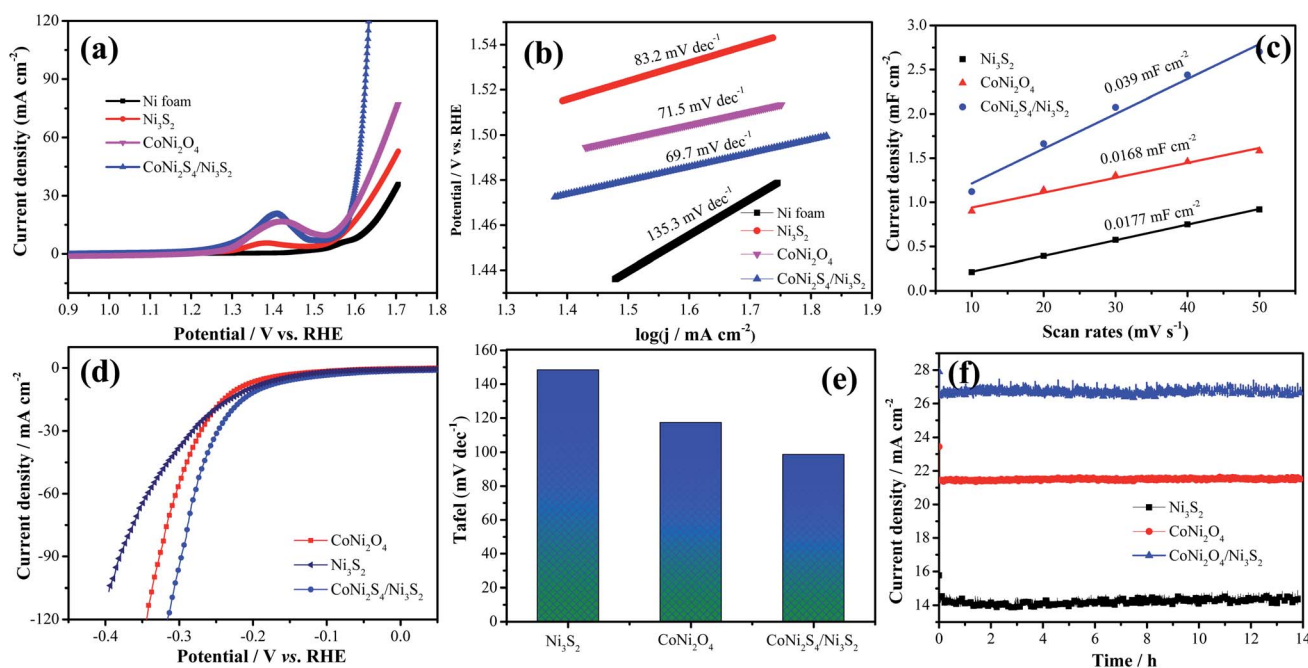

Fig. 7 (a–c) OER of the as-prepared catalysts, (a) LSV curves, (b) Tafel, (c) electric double layer capacitor value, (d) LSV curves for HER, (e) Tafel for HER, (f) cycle stability.
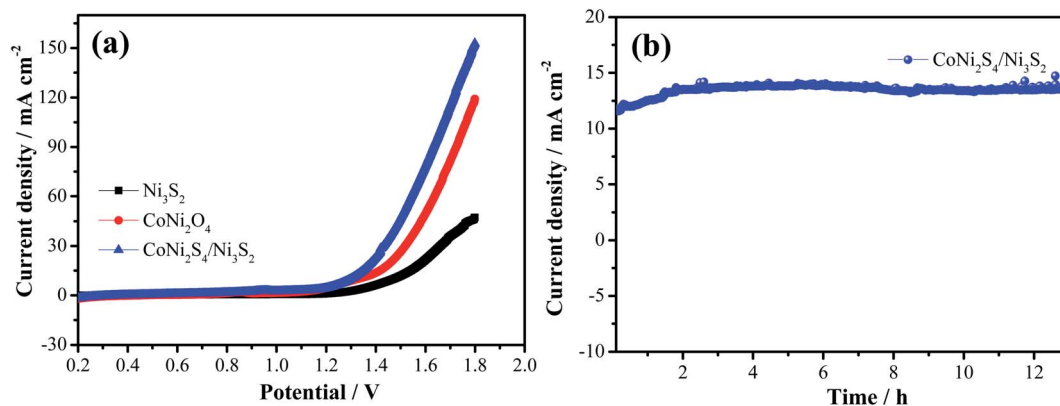
Fig. 8 Overall water splitting of the as-prepared samples. (a) LSV curves, (b) cycle stability.

layer capacitance (C_{dl}). The value of the electrochemical double layer capacitance is shown in Fig. 7c. $CoNi_2S_4/Ni_3S_2$ nanowires exhibit a higher ECSA (0.039 mF cm^{-2}) than $CoNi_2O_4$ nanowires (0.0168 mF cm^{-2}) and Ni_3S_2 samples (0.0177 mF cm^{-2}). The HER performance of the as-prepared samples is also tested at 5 mV s^{-1}. The comparison of the LSV curves of catalysts is depicted in Fig. 7d. It is clearly found that hybrid $CoNi_2S_4/Ni_3S_2$ nanowires exhibit a small Tafel slope of 173.8 mV at −10 mA cm^{-2}, which is lower than that of $CoNi_2O_4$ nanowires (192.6 mV) and Ni_3S_2 samples (210.8 mV). Fig. 7e shows the corresponding Tafel plots, which shows that hybrid $CoNi_2S_4/Ni_3S_2$ nanowires exhibit a small Tafel slope of 98.8 mV dec^{-1}, which is lower than the $CoNi_2O_4$ nanowires (117.2 mV dec^{-1}) and Ni_3S_2 samples (148.9 mV dec^{-1}). The Tafel slope of $CoNi_2S_4/Ni_3S_2$ nanowires is smallest, revealing the fast reaction kinetics. Since the Tafel slope is in the range from 40 to 120 mV dec^{-1}, this implies that the HER reaction of $CoNi_2S_4/Ni_3S_2$ nanowires obey the Volmer–Heyrovsky mechanism, and the Volmer step is rate-determining.[36] The long-term stability measurements of the three electrode materials are conducted at a constant potential for 13 h, as shown in Fig. 7f. The results demonstrate that the as-fabricated catalysts present excellent cycle stability.

To further investigate the potential practical applications, overall water splitting tests are conducted through a two-electrode system with the hybrid structured catalysts as both the cathode and anode. Fig. 8a presents the LSV curve of overall water splitting with a scan rate of 5 mV s^{-1}. It is seen that hybrid $CoNi_2S_4/Ni_3S_2$ samples show a small cell voltage of 1.43 V at 30 mA cm^{-2}, which is lower than that of $CoNi_2S_4$ nanowires (1.51 V) and Ni_3S_2 samples (1.65 V). In order to evaluate the stability of the as-prepared catalysts, chronoamperometry measurements were conducted, as depicted in Fig. 8b. It was found that the hybrid structured $CoNi_2S_4/Ni_3S_2$ samples possess excellent long durability. At the same time, a large number of bubbles were formed from both the cathode and anode as the electrocatalytic test proceeded.

4. Conclusion

In summary, hybrid structured $CoNi_2S_4/Ni_3S_2$ nanowires were fabricated through a facile two-step hydrothermal method. The

as-prepared products directly act as a supercapacitor electrode with a specific capacitance of 997.2 F g^{-1} at 1 A g^{-1} and cycle stability of 80.3% retention after 5000 cycles. The asymmetric supercapacitor shows a high energy density of 0.4 mW h cm^{-3} at a power density of 3.99 mW cm^{-3} and cycling stability of 79.2% retention after 10 000 cycles. The as-fabricated $CoNi_2S_4/Ni_3S_2$ nanowires also exhibit excellent electrocatalytic performance with a low overpotential of 360 mV for the OER and a small Tafel slope of 98.8 mV dec^{-1} and a cell voltage of 1.43 V.

Conflicts of interest

The authors declare no conflict of interest.

Acknowledgements

References

1 F. Shahzad, M. Alhabeb, C. B. Hatter, B. Anasori, S. Man Hong, C. M. Koo and Y. Gogotsi, *Science*, 2016, **353**, 1137–1140.

2 D. F. Yan, Y. X. Li, J. Huo, R. Chen, L. M. Dai and S. Y. Wang, *Adv. Mater.*, 2017, **29**, 1606459.

3 J. Y. Rao, N. S. Liu, Z. Zhang, J. Su, L. Y. Li, L. Xiong and Y. H. Gao, *Nano Energy*, 2018, **51**, 425–433.

4 Q. Q. Qin, D. W. Ou, C. J. Ye, L. X. Chen, B. B. Lan, J. Yan and Y. C. Wu, *Electrochim. Acta*, 2019, **305**, 403–415.

5 Y. Li, J. Xu, T. Feng, Q. F. Yao, J. P. Xie and H. Xia, *Adv. Funct. Mater.*, 2017, **27**, 1606728.

6 M. Dakshana, S. Meyvel, M. Malarvizhi, P. Sathya, R. Ramesh, S. Prabhu and M. Silambarasan, *Vacuum*, 2020, **174**, 109218.

7 M. R. Lukatskaya, B. Dunn and Y. Gogotsi, *Nat. Commun.*, 2016, **7**, 12647.

8 L. X. Xu, S. S. Xiong, S. X. Zhong, S. Bai, Y. Jiao and J. R. Chen, *Vacuum*, 2020, **174**, 109213.

9 J. Tian, Q. Liu, A. M. Asiri and X. Sun, *J. Am. Chem. Soc.*, 2014, **136**, 7587–7590.

10 J. Kim, Y. Lee and S. Sun, *J. Am. Chem. Soc.*, 2010, **132**, 4996–4997.

11 Y. L. Zhou, D. Y. Lin, X. Y. Ye and M. Y. Zhu, *J. Alloys Compd.*, 2020, **839**, 155691.

12 Y. Zhao, R. Nakamura, K. Kamiya, S. Nakanishi and K. Hashimoto, *Nat. Commun.*, 2013, **4**, 2390.

13 S. Bai, C. Wang, M. Deng, M. Gong, Y. Bai, J. Jiang and Y. Xiong, *Angew. Chem., Int. Ed.*, 2014, **53**, 12120–12124.

14 K. A. Stoerzinger, L. Qiao, M. D. Biegalski and Y. Shao-Horn, *J. Phys. Chem. Lett.*, 2014, **5**, 1636–1641.

15 Y. Pi, Q. Shao, P. Wang, J. Guo and X. Huang, *Adv. Funct. Mater.*, 2017, **27**, 1700886.

16 S. M. Jasem and A. C. C. Tseung, *J. Electrochem. Soc.*, 1979, **126**, 1353–1360.

17 Z. Yang, H. Lv and R. Wu, *Nano Res.*, 2016, **9**, 3671–3682.

18 Y. Cheng, H. Zhao, H. Lv, T. Shi, G. Ji and Y. Hou, *Adv. Electron. Mater.*, 2020, **6**, 1900796.

19 R. Chen, H. Y. Wang, J. W. Miao, H. B. Yang and B. Liu, *Nano Energy*, 2015, **11**, 333–340.

20 S. J. Peng, L. L. Li, C. C. Li, H. T. Tan, R. Cai, H. Yu, S. Mhaisalkar, M. Srinivasan, S. Ramakrishna and Q. Y. Yan, *Chem. Commun.*, 2013, **49**, 10178–10180.

21 R. Li, S. L. Wang, Z. C. Huang, F. X. Lu and T. B. He, *J. Power Sources*, 2016, **312**, 156–164.

22 J. Liu, J. S. Wang, B. Zhang, Y. J. Ruan, L. Lv, X. Ji, K. Xu, L. Miao and J. J. Jiang, *ACS Appl. Mater. Interfaces*, 2017, **9**, 15336–15345.

23 L. J. Deng, P. H. Zhou, J. L. Xie and L. Zhang, *J. Appl. Phys.*, 2016, **101**, 103916.

24 G. He, J. Li, W. Li, B. Li, N. Noor, K. Xu, J. Hu and I. P. Parkin, *J. Mater. Chem. A*, 2015, **3**, 14272–14278.

25 H. Lv, X. Liang, Y. Cheng, H. Zhang, D. Tang, B. Zhang, G. Ji and Y. Du, *ACS Appl. Mater. Interfaces*, 2015, **7**, 4744–4750.

26 X. Liu, C. Hao, L. He, C. Yang, Y. Chen, C. Jiang and R. Yu, *Nano Res.*, 2018, **11**, 4169–4182.

27 X. J. Chen, D. Chen, X. Y. Guo, R. M. Wang and H. Z. Zhang, *ACS Appl. Mater. Interface*, 2017, **9**, 18774–18781.

28 B. Y. Guan, L. Yu, X. Wang, S. Song and X. W. Lou, *Adv. Mater.*, 2017, **29**, 1605051.

29 Q. Wu, J. Wang, H. Jin, T. Yan, G. Yi, X. Su, W. Dai and X. Wang, *Mater. Lett.*, 2018, **244**, 138–141.

30 Y. Z. Wu, J. S. Meng, Q. Li, C. J. Niu, X. P. Wang, W. Yang, W. Li and L. Q. Mai, *Nano Res.*, 2017, **10**, 2364–2376.

31 Y. L. Tong, X. Y. Cheng, X. Y. Liu, D. L. Qi, B. Q. Chi and Y. F. Wang, *J. Nanoelectron. Optoelectron.*, 2020, **15**, 237–242.

32 Y. L. Tong, D. L. Qi, B. Q. Chi and W. Q. Zhang, *Sci. Adv. Mater.*, 2019, **11**, 338–344.

33 S. S. Xiong, S. Y. Jiang, J. Wang, H. J. Lin, M. X. Lin, S. T. Weng, S. Liu, Y. Jiao, Y. C. Xu and J. R. Chen, *Electrochim. Acta*, 2020, **340**, 135956.

34 Y. L. Tong, B. Q. Chi, D. L. Qi and X. Y. Liu, *Sci. Adv. Mater.*, 2019, **11**, 1087–1092.

35 Y. Sun, K. Xu, Z. Wei, H. Li, T. Zhang, X. Li, W. Cai, J. Ma, H. J. Fan and Y. Li, *Adv. Mater.*, 2018, **30**, 1802121.

36 L. Huang, D. Chen, G. Luo, Y. Lu, C. Chen, Y. Zou, C. Dong, Y. Li and S. Wang, *Adv. Mater.*, 2019, **31**, 1901439.